# Ammonia Decomposition on Lithium Imide Surfaces: A New Paradigm in Heterogeneous Catalysis

**Manyi Yang, Umberto Raucci, Michele Parrinello***
Italian Institute of Technology
Via E. Melen 83, Genoa, 16152, Italy
michele.parrinello@iit.it

**Abstract**

The industrial production of commodity chemicals often requires extreme conditions of temperature and pressure [1]. Yet, in industrial reactors the catalyst remains active for a long time notwithstanding the harsh operating conditions. This challenges a static picture of the catalytic process. To explain the long-term stability of the industrial catalysts we invoke instead a highly dynamical scenario. We illustrate this concept with an *ab initio* quality simulation of the $Li_2NH$ catalyzed decomposition of ammonia [2, 3] at $T = 750$ K. This process has been intensively studied for its possible use in a hydrogen-based economy [4, 5, 6, 7, 8, 9]. However, a full understanding of the way it works is still lacking. We show that when exposed to the reactants, the surface structure of the catalyst changes and a dynamic fluctuating steady state is activated allowing the reaction to proceed until the flow of reagents is discontinued. This interfacial reactive fluctuating state is induced by the reaction of ammonia with the surface imides $NH^{2-}$ + $NH_3 \rightarrow 2NH_2^-$. This discommensuration induces large fluctuations in the top surface layers, which now behave almost like an ionic liquid. In this activated environment, a series of reactions that eventually lead to the release of $N_2$ and $H_2$ molecules become possible.

Lithium imide ($Li_2NH$) [10] is an ionic compound whose structural arrangement is dominated by the need to alternate divalent ($NH^{2-}$) anions and monovalent $Li^+$ cations (Fig. 1**a**) in order to establish local charge neutrality. The experimentally reported defective antifluorite structure does reflect this building principle [11, 12, 13]. Like many other ionic systems [14] in which there is a large difference between anionic and cationic radii, it exhibits a superionic behaviour [15, 16] in which the small $Li^+$ cations have a high diffusion coefficient, while the divalent anions oscillate around their equilibrium positions (Fig. 1**b**). The transition to the superionic state is facilitated by the ease with which octahedral lithium interstitial can be formed.

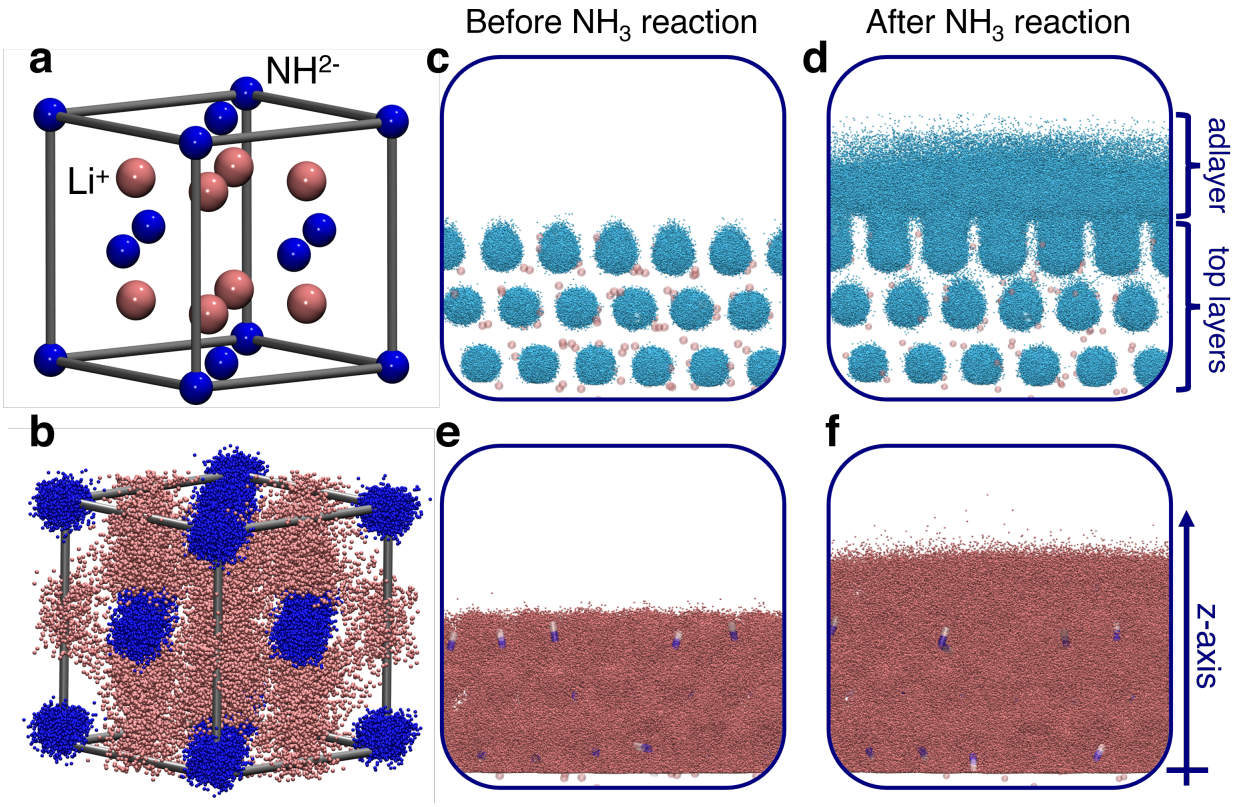


Figure 1: **Bulk and surface structure of $Li_2NH$**. (**a**) Antifluorite structure of $Li_2NH$. The sublattice of $NH^{2-}$ divalent anions is face centered cubic (FCC) whereas the $Li^+$ cations occupy the tetrahedral sites. Hydrogen atoms are omitted for clarity in panel (**a**) and in the following panel (**b**). (**b**) Scatter plot of N and Li atoms positions in one of the primitive cells of the simulated $Li_2NH$ crystal at 600 K. Frames are reported every 1.6 ps during a 5 ns long trajectory. Scatter plots of N (**c-d**) and Li (**e-f**) atoms positions during 0.8 $\mu$s long trajectories at $T = 750$ K before (**c, e**) and after (**d, f**) the reaction with ammonia. In panel (**c-d**) and (**e-f**) we report a frame every 1 and 10 ps, respectively. The nitrogen atoms of the three top layers are plotted in panel (**c**), while the adlayer resulting from the ammonia reaction with the surface is also shown in panel (**d**). In panel (**e**) and (**f**) we plot only lithium atoms that have a value of the $z$ coordinate higher than the one marked in panel (**f**). This corresponds to choosing $Li^+$ cations that are either in the top three layers (**e**) and/or in the adlayer (**f**). To simplify reading, a single instantaneous configuration is chosen to represent N and H atoms. Li, N and H atoms are coloured pink, blue, and white, respectively.

In order to simulate the catalytic process, one needs to perform a molecular dynamics simulations in which the interatomic forces are computed from accurate electronic structure calculations so as to properly describe the forming or breaking of chemical bonds [17]. Unfortunately, such an endeavour is still computationally too expensive.

However, following the pioneering work of Behler and Parrinello [18] we constructed an *ab initio* quality reactive force field by training a feed-forward neural network [19] to reproduce total energies and forces computed using Density Functional Theory [20] (DFT), and in particular we use here the PBE exchange and correlation functional [21]. The training configurations were chosen using an active learning approach similar to that of Ref. [22, 23, 24, 25]; a description of the procedure adopted can be found in the Method Section. During both training and simulation, we used state-of-the-art enhanced sampling methods [26, 27] to generate reactive events in an affordable computational time. The potential thus trained correctly reproduces the experimental $Li_2NH$ superionic behaviour (see Supplementary Information (SI) Fig. S6).

Since it is not known which surface is the most active one, we have taken a conservative approach and chosen to study the $(111)$ cleavage surface at the *operando* temperature of $T = 750$ K. We expect that, if a dynamical scenario applies when the most stable surface is considered, *a fortiori* less stable surfaces would exhibit a similar, if not even more dynamical behaviour. A validation of this assertion can be found in the SI (Fig. S8 and S9), where we study how the catalysis proceeds on the $(001)$ surface.

In our simulation the $(111)$ surface remains stable including the outermost layers (Fig. 1**c,e** and Fig S7). Since at 750 K the catalyst is in the superionic phase, anions fluctuate around their equilibrium positions while cations diffuse rapidly (SI video 1). However, the behaviour of the surface changes dramatically when we let two ammonia molecules approach the surface so as to study the stochiometric reaction $2NH_3 \rightarrow N_2 + 3H_2$. On a time scale of nanoseconds the two ammonia molecules react with two imides to give a total of four amides according to: $2NH^{2-} + 2NH_3 \rightarrow 4NH_2^-$ (SI video 2). This agrees with the experimental report that this is the first step in the cracking process [2]. As a consequence of this reaction two doubly charged $NH^{2-}$ anions are transformed into four singly charged $NH_2^-$ ones. After the reaction, the surface struggles to orderly accommodate the change in the number and charge of the anions and this leads to a novel dynamical behavior. Two amides move to the adlayer accompanied by some of the $Li^+$ while the two remaining amides replace two imides in the top layer (Fig. 1**d,f** and and Fig S7). Apart from short-lived fluctuations, this amide distribution is preserved during the simulation. From Fig.1**d** and Fig. S7 it clearly transpires that both amide and imide anions now exhibit a diffusive behaviour and amide diffuses faster than imide (SI videos 3 and 4). In addition, on the time scale of nanoseconds protons can be exchanged between amides and imides (SI videos 5). Such Grotthus-like events have also been experimentally detected [2, 28]. These changes are confined to the top two layers that now has a behavior akin to that of an ionic liquid. The present picture is consistent with the finding that non-stochiometric compounds like $Li_{2-x}(NH_2)_x(NH)_{1-x}$ have an increased activity [29, 28]. In fact, the disorder, in particular charge disorder, will favor the formation of the activated dynamical state that is at the heart of this catalytic process.

In this destabilized environment many reactions become possible. Discovering them all is extremely challenging and in a sense is beyond the scope of the present paper. To prove our point we only need to show that in the reactant induced scenario there are plausible pathways for the ammonia decomposition. Several likely reaction steps are reported in the SI in a list that is far from exhaustive. All these steps have been discovered using our enhanced sampling method [26, 27] (see Method Section), and imposing that their free

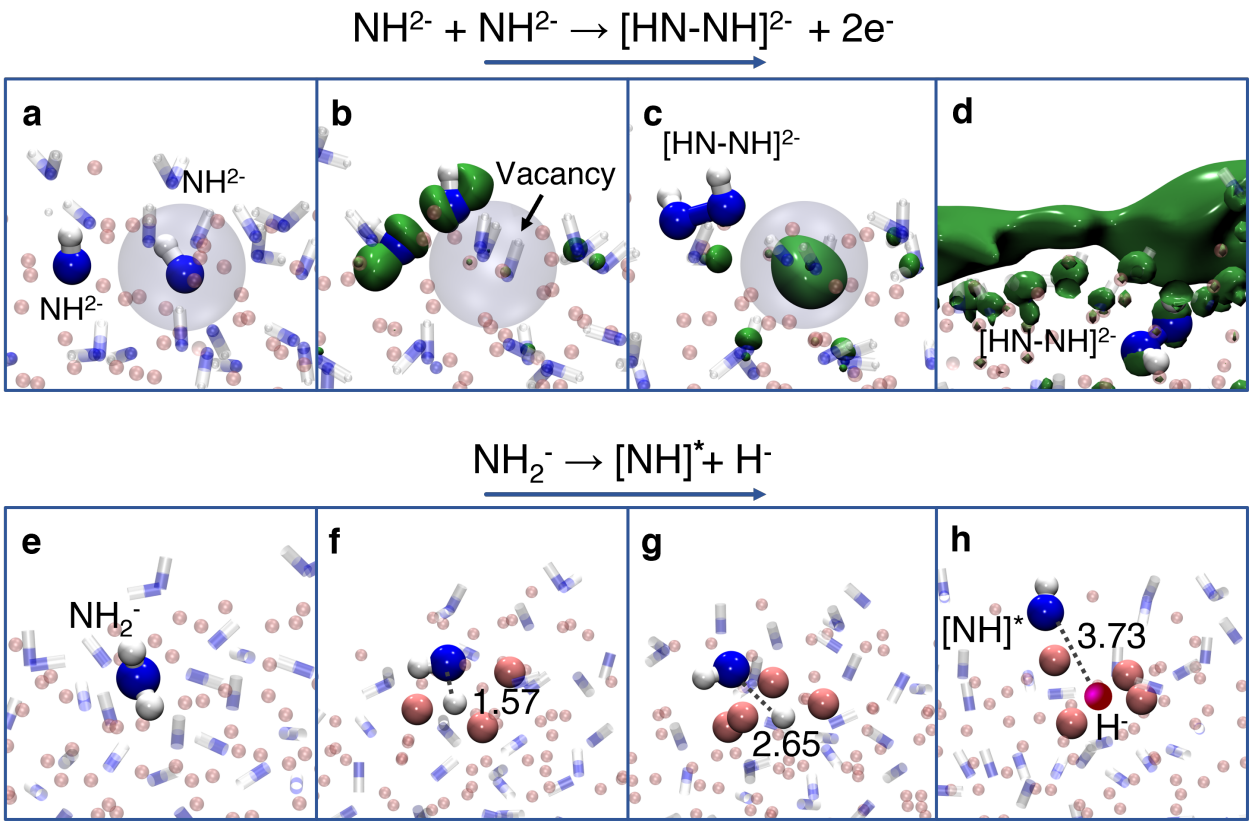


Figure 2: **Schematic representation of the initial reaction steps.** (**a-d**) Formation of the diazanediide anion ($[HN\text{-}NH]^{2-}$) according to: $NH^{2-} + NH^{2-} \rightarrow [HN\text{-}NH]^{2-} + 2e^{-}$. The position of one $NH^{2-}$ before the reaction is marked with a grey transparent sphere (**a**). As the two $NH^{2-}$ come close the $[HN\text{-}NH]^{2-}$ is formed and an ionic vacancy is left behind (**b**). The resulting cavity can localize the two electrons resulting from the $[HN\text{-}NH]^{2-}$ formation (**c**). These two electrons can also be accommodated in a diffuse surface state (**d**). In panel (**b-d**) the HOMO orbital is shown as green solid isosurface. (**e-h**) Formation of the hydride ($H^{-}$) ion according to: $NH_2^{-} \rightarrow [NH]^{*} + H^{-}$. An amide ion (**e**) is progressively stripped of one proton helped by the intervention of the $Li^{+}$ cations which stabilize the resulting $H^{-}$ (**f-h**). In panel (**f-h**) the N-H bond length (Å) is reported in black, and lithium atoms within 2.5 Å from the H atom are shown. Li, N, H and $H^{-}$ are coloured pink, blue, white, and purple, respectively.

energy barriers are low enough for the reaction to take place at the *operando* temperature (Table S1). Different steps can be concatenated in many different ways so as to eventually lead to the desired products (Fig. S12). Of course the ability of the catalyst to choose between different pathways increases its efficiency.

Here, we describe only two initial reaction steps that are paradigmatic of the way the activated ionic top layers catalyze reactions that would otherwise have been impossible. One of the initial steps leads the formation of the diazanediide ($[HN\text{-}NH]^{2-}$) anion via the reaction $NH^{2-} + NH^{2-} \rightarrow [HN\text{-}NH]^{2-} + 2e^{-}$ (Fig. 2**a-b** and SI video 6). The highly fluxional ionic interlayer allows this reaction because the diazanediide is stabilized by a cloud of $Li^{+}$ cations (Fig. S13), and the two product electrons can be accommodated either in a diffuse surface state or in a state localized in an imide vacancy (Fig. 2**c-d**). One can liken this second localized state to that of a color centre in ionic crystals. Interestingly, recent experiments on ammonia decomposition on a CaNH-supported catalyst have

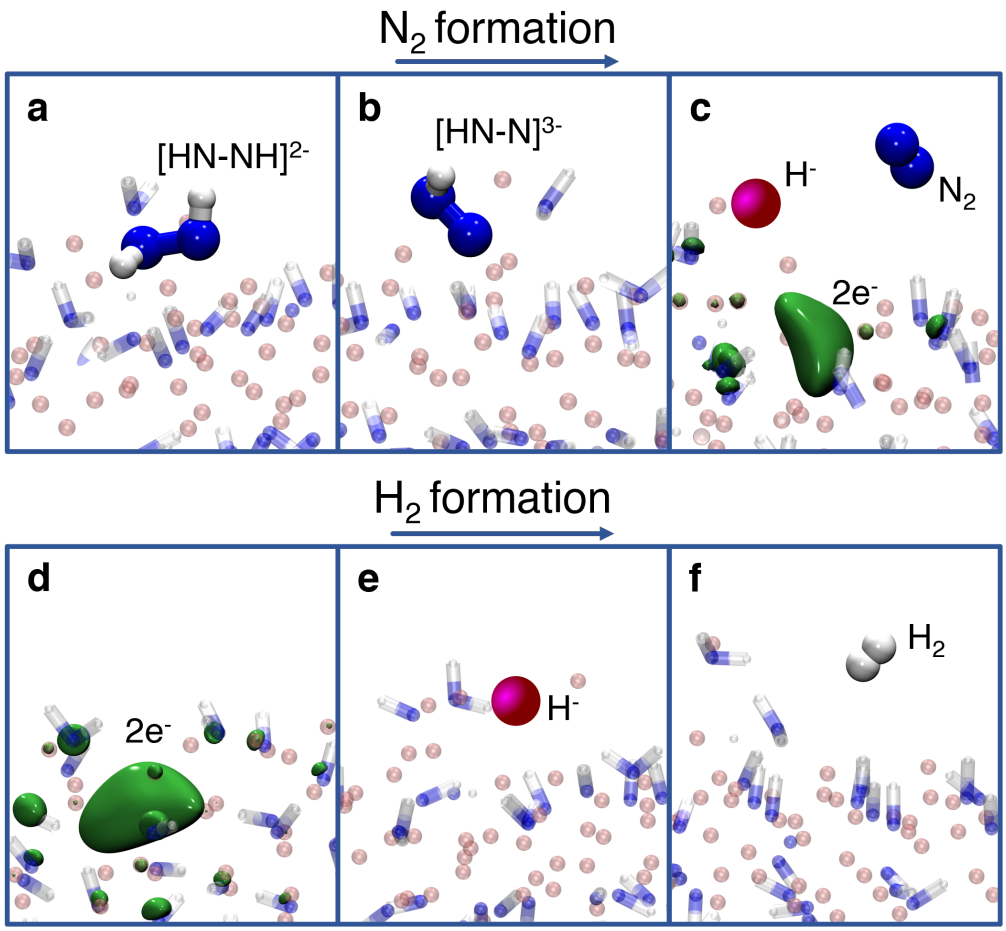


Figure 3: **Schematic of one representative set of decomposition reactions**. The diazanediide anion (**a**) loses one proton forming diazanetriide $[N\text{-}NH]^{3-}$(**b**) which can finally lead to $N_2$ (**c**). In addition, the solvated two electron state (**d**) can abstract a proton from the nitrogen hydrides species forming $H^-$ (**e**). The release of molecular hydrogen (**f**) from the hydride anion is then possible due to its strong basic character. In panel (**b-d**) the HOMO orbital is shown as green solid isosurface. Li, N, H and $H^-$ are coloured pink, blue, white, and purple, respectively.

suggested that color centres play a role also in this catalytic process [30]. The solvated two electron state fluctuates from its diffuse to its localized variant (Fig. S10).

Another pathway to the formation of the diazanediide starts with the abstraction of $H^-$ from an amide. Such a reaction would have be impossible in the gas phase but here is made possible by the $Li^+$ intervention (Fig. 2**e-h** and SI video 7) that facilitate the breaking of the bond, and the subsequent stabilization of $H^-$. An unusual polaronic intermediate state $[NH]^*$ is then formed. If we analyze this state using the Bader charges [31] we see that about two negative charges are associated to the [NH] while a compensating positive charge is distributed among the nitrogen atoms (Fig. S11). This $[NH]^*$ intermediate reacts with an imide leading to the formation of a diazanediide. Thus, the overall reaction can be read as $NH_2^- + NH^{2-} \rightarrow [HN\text{-}NH]^{2-} + H^-$.

The three species $[HN\text{-}NH]^{2-}$, $2e^-$ and $H^-$ then become the main actors in the reactions that follow. In one set of reactions the diazanediide is progressively stripped of its

protons, eventually leading to the formation and release of an $N_2$ molecule (Fig. 3**a-c**). The solvated $2e^-$ can abstract a proton from any of the nitrogen hydrides following the scheme $2e^-$ + $NH_x^{(3-x)-} \rightarrow NH_{x-1}^{(3-(x-1))-}$ + $H^-$. Finally, the presence of the $H^-$ intermediate, in whichever way it is formed, is essential to the release of an $H_2$ molecule after reacting with a nitrogen hydrides species [32, 16] (Fig. 3**d-f**).

We must emphasize that the ability of the activated $Li_2NH$ surface to supply and accept protons and/or electrons as the reaction proceeds is crucial to its catalytic function. In this respect, it is interesting to note that in building ammonia molecules, the nitrogenase enzyme follows a strategy in which proton and electron exchanges are appropriately coordinated [33, 34].

If we look at this process from a loftier standpoint we see that the highly dynamical behaviour induced by the first step in the ammonia decomposition is what eventually leads to catalysis, and it is the surface and its subsurface volume that act as a catalyst, not this or that atomic configuration. However, once started the process is self sustained with the different reaction steps further contributing to the surface dynamical behaviour and therefore to its catalytic efficiency. Once the catalyst is no longer exposed to ammonia, the reaction stops, and the catalyst returns to its original state. This system combines the benefit of a heterogeneous catalyst with a surface behavior similar to that of a homogeneous one. Our picture is far more radical than number of proposals made to model catalyst activity as resulting from the presence of different metastable states [35, 36]. We have in fact discovered that during the reactions the interface undergoes a very dramatic change and has properties different from those of the pristine surface.

In conclusion, our simulation is a vindication of the statement made by Ertl in his Nobel address that a sampling approach is needed to understand catalytic processes [37]. Luckily we are now in the position to make his vision come true. This and the progress *in operando* experiments will allow the field of heterogeneous catalysis to be moved from black magic to science. From our simulation, it is clear that catalysis is a highly complex process. Only by taking complexity into consideration real progresses can be made. It is hoped that this novel insight can lead to the rational design of more efficient catalysts.

## Methods

The superionic behaviour of $Li_2NH$ was studied in a cubic supercell of edge 20.028 Å, containing 1024 atoms which amounts to replicate $2 \times 2 \times 2$ times the conventional unit cell [38] (Fig. S1**a**). The ammonia decomposition on the $(111)$ surface was modeled using a slab made of 384 atoms in a monoclinic simulation box with edges $14.321, 14.321, 30.0$ Å, and $\gamma = 120^\circ$ (Fig. S1**b**). In this setup we left enough distance (about 15 Å) between replicas along the $z$ direction to minimize interactions. In all the simulations of the $(111)$ surface we fixed the atoms in the two bottom layers to their ideal crystal lattice positions to mimic the bulk environment.

We also studied the $(001)$ surface with two possible terminations: $Li^+$ (Fig. S2**a**), and $NH^{2-}$ (Fig. S2**b**). Since this is a charged surface care is required to set it up. To restore neutrality we followed the procedure described in Ref. [39], and moved half of the $Li^+$ or $NH^{2-}$ ions from the outermost layer to the bottom one. Finally, we relaxed the whole structure. This led to a reconstruction of the top layer similar to what can be found in compounds like MgO [40]. This slab was made of 480 atoms in a tetragonal simulation cell with edges $15.95, 15.95, 30$ Å. This amounted to imposing a distance of about 15.0 Å between one slab and its periodic replicas in the $z$ direction. During the molecular dynamics (MD) simulations we kept fixed the atoms in the bottom three layers.

We introduced two $NH_3$ molecules in the simulation box to study the ammonia decomposition reaction. To restraint the movement of the N atoms close to the surface, we limited $d_z$, the $z$ component of the maximum distance between the N atoms and a ghost atom with $xyz$ coordinates $0.0, 0.0, 15.0$ Å, to be smaller than $d_0 = 12$ Å. This is done by applying an harmonic restraint of the form $k/2(d_z\text{-}d_0)^2$ with $k/2 = 2000$ kJ/mol.

In the calculation of DFT energies and forces we used two different packages. *Ab initio* molecular dynamics (AIMD) simulations were performed using the Quickstep [41] module of the CP2K package [42] supplemented by the PLUMED 2.8 plugin [43], while the energies and forces needed for the Neural Network (NN) training were calculated using the PWSCF v.7.0 code from the Quantum Espresso package [44, 45, 46]. This latter was used to check the effect of the Brillouin zone $k$-points sampling. We satisfied ourselves that use of Γ-point only was appropriate as expected. We checked that our NN can reproduce well also the CP2K forces.
We characterized the electronic states along the reaction pathways by computing eigenvalues, eigenfunctions and Bader charges [31] on representative configurations extracted from NN-based molecular dynamics. These calculations were performed using Quantum Espresso.
In the next sections all the simulation details are provided.

### AIMD simulations

All the AIMD simulations were performed in the canonical ensemble (NVT) with periodic boundary conditions, and a time step of 0.5 fs. The temperature was controlled using the stochastic velocity rescaling thermostat [47] with a coupling constant of 0.05 ps. Energy and forces were computed using the Perdew–Burke–Ernzerhof (PBE) exchange-correlation functional [21]. The Kohn-Sham orbitals were expanded in a triple-$\zeta$ plus

polarization (TZVP) Gaussian basis sets and the plane wave expansion of the electronic density was truncated at an energy cutoff of 300 Ry. The core electrons were treated using the Goedecker-Teter-Hutter (GTH) pseudopotentials [48, 49] optimized for PBE. The AIMD simulations were performed on the $(001)$ surface. This slab was made of 256 atoms in a tetragonal simulation cell [12] with edges $10.087, 10.087, 33$ Å.

**Calculation of energies and forces**

The DFT energies and forces needed for the NN training were calculated using again the PBE exchange-correlation functional. The RRKJUS PBE pseudopotentials taken from the QE pseudopotential library were used. The Kohn-Sham orbitals were expanded in plane waves basis set up to a kinetic-energy cutoff of 80 Ry and a density cutoff at 400 Ry. The convergence threshold for self-consistency was set to $1.0 \times 10^{-7}$ a.u..

**NN-based MD**

The MD simulations that used the NN potential were performed by patching the DeepMD-kit software [50] implemented in LAMMPS [51] and PLUMED 2.8 [43]. The canonical ensemble (NVT) was sampled in all the simulations, controlling the temperature with the stochastic velocity rescaling thermostat [47] with a coupling constant of 0.02 ps. A time step of 0.25 fs was used.

**Enhanced sampling method: OPES**

We used enhanced sampling simulations to explore the $NH_3$ decomposition reactions. Our strategy was based on enhancing the fluctuations of a set of carefully selected collective variables (CVs) $\mathbf{s}$=$\mathbf{s}(\mathbf{R})$ where $\mathbf{R}$ are the atomic coordinates. The CVs encoded the difficult to sample degrees of freedom of the system. We used the on-the-fly probability enhanced sampling (OPES) method to enhance the fluctuations of $\mathbf{s}$. In OPES, the equilibrium probability distribution $P(\mathbf{s})$ is first estimated on-the-fly, and then a bias potential $V_n(\mathbf{s})$ is constructed so as to converge the $\mathbf{s}$ distribution to a target one $P^{tg}(\mathbf{s})$.

Here, we used as target distribution the well-tempered one $P^{tg}(\mathbf{s}) \propto [P(\mathbf{s})]^{\frac{1}{\gamma}}$, where $\gamma > 1$ is the bias factor, and $\beta = 1/k_B T$. In this case, the bias potential at $n^{th}$ iteration is written as:

$$V_n(\mathbf{s}) = (1 - 1/\gamma)\frac{1}{\beta}\log\left(\frac{P_n(\mathbf{s})}{Z_n} + \epsilon\right) \tag{1}$$

where $Z_n$ is a normalization factor, and $\epsilon = \mathrm{e}^{-\beta\Delta E/(1-1/\gamma)}$ is a regularization parameter that limits the maximum bias that can be deposited. This allows only the lowest free energy pathways to be explored avoiding the less likely higher energy reactions. The highest value of $\Delta E$ used was 200 kJ/mol. However, to generate the training configurations as described in the next section, we used larger values of $\Delta E$ (up to 300 kJ/mol) which allowed the generation of less likely configurations, thus increasing the robustness of the NN potential.

As in all the CV based enhanced sampling methods, also in OPES a good choice of the CVs is extremely important. When choosing the CVs, we tried as much as possible

not to prejudge the outcome of the reaction, nor the identity of the atoms involved. A quantity that we found useful in the CV definition is the coordination number written as a continuous function in order to avoid discontinuities when calculating the forces coming from the bias:

$$C_{i\in A}^{B} = \sum_{j\in B}^{N_j} \frac{(1-\frac{d_{ij}}{r_0})^n}{(1-\frac{d_{ij}}{r_0})^m} \tag{2}$$

In the above equation, $d_{ij}$ is the distance between atoms $i$ and $j$, $\mathrm{N}_j$ is the number of atoms of species $B$, and the exponents $n$ and $m$ control the sharpness of the function. Here, we set $n = 6$ and $m = 12$. Thus, $C_i^B$ measures how many atoms of species $B$ are within a sphere of radius $r_0$ centred on atom $i$, and it allows forming or cleaving chemical bonds.

Depending on the circumstances, we use as CV the following combination of $C_i^B$:

$$S_{AB} = \sum_{i\in A} C_i^B \tag{3}$$

$$S_{AB}^{max} = \alpha \log \sum_{i\in A} \exp\left(\frac{C_i^B}{\alpha}\right) \tag{4}$$

$$S_{AB}^{min} = \frac{\beta}{\log \sum_{i\in A} \exp\left(\frac{C_i^B}{\beta}\right)} \tag{5}$$

$S_{AB}^{max}$ and $S_{AB}^{min}$ are soft max and soft min functions that select the atoms with the highest and lowest coordination number, respectively.

We used a sequential strategy to discover the set of reactions that led to $\mathrm{N}_2$ and $\mathrm{H}_2$. After a novel reaction step was discovered, we took the newly discovered species and applied the CV that was most appropriate for the reaction to proceed. In Table S1 we list the CVs and biases $\Delta E$ used, together with the products that these CVs have helped discovering. These CVs were used in both the NN training and production simulations.

**NN training**

The NN potentials was trained using the Deep Potential-Smooth Edition scheme [52] as implemented in the DeePMD-kit package [50]. This model consists of two neural networks: the embedding and the fitting one. Both networks use the ResNet architecture [53]. We chose an embedding network with three hidden layers and $(30, 60, 120)$ nodes/layer. The size of the embedding matrix has been set to 16. Four hidden layers with $(240, 240, 240, 240)$ nodes/layer were used in the fitting network. The cutoff radius was set to 8.0 Å and the descriptors decay smoothly from 0.5 Å to 8.0 Å. The learning rate decays from $1.0 \times 10^{-3}$ to $5.0 \times 10^{-8}$. The batch size was set to 8. The following loss function was minimized during training:

$$L(\alpha_E, \alpha_f, \alpha_\xi) = \alpha_E \, \Delta E^2 + \frac{\alpha_f}{3N} \sum_i \Delta \mathbf{F}_i^2 + \frac{\alpha_\xi}{9} \|\Delta \xi\|^2 \tag{6}$$

where $\alpha_E, \alpha_f, \alpha_\xi$ are the energy force and the virial tensor prefactors, respectively. $\Delta$ denotes the difference between the DeePMD prediction of the energy, forces and virial and the training data, $N$ is the number of atoms, $E$ is the energy per atom, $\mathbf{F}_i$ is the force on atom i, and $\xi$ is the virial tensor$= -\frac{1}{2}\sum_i \mathbf{R}_i \otimes \mathbf{F}_i$. The prefactors of the energy and force terms in the loss function changed from 0.05 to 5 and from 1000 to 1, respectively. The virial term was also included in the loss function with prefactor value changing from 0.01 to 1. In the initial training phase $1.0 \times 10^6$ training steps were used. In order to obtain the final NN model this number was doubled.

**Setting up the training set**

The construction of the NN potential for such a multi-component reactive system is the most challenging part of the work, and requires a careful balance between computational effort and sufficient coverage of the configuration space. In our case, this is made harder by the fact that we have to model a highly reactive system, and therefore many rare but critical events need to be explored, and the potential energy for these events accurately predicted.

An active learning approach assisted by the enhanced sampling method OPES [26, 27] was used to explore the relevant configurations involved in the $NH_3$ decomposition process (Fig. S3). This strategy has already been successfully applied to study several other complex systems [22, 23, 25, 24].

First, we used about 3900 atomic configurations from the AIMD simulations performed on the smaller 256 atoms system described above representing the (001) surface, and built an initial training set. About 70 short AIMD simulations ranging from 1 to 6 ps were performed at the temperatures of 600 K, 700 K, and 750 K.
As the NN potential building proceeded we added configurations taken from the (111) surface. Our active learning procedure made sure that we considered reactive configurations.
The OPES method has been adopted to enhance the exploration of possible reactive configurations and reaction pathways. Starting from these configurations and the associated DFT energies and forces, we have followed an active learning approach (Fig. S3) to extend and refine the training set. Each active learning iteration involved the following steps:

**Step 1:** Four NN potentials using different initial weights were trained based on the same training set as the previous iteration;

**Step 2:** A series of NN-based OPES simulations were performed to explore new relevant atomic configurations and reaction pathways. We computed for each configuration a local estimate of the reliability of the NN. This was measured by $\sigma$ [54], defined as the maximal standard deviation of the atomic forces predicted by these four NN potentials:

$$\sigma = \max_i \sqrt{\frac{1}{4}\sum_{\alpha=1}^{4} \|\mathbf{F}_i^\alpha - \overline{\mathbf{F}_i}\|^2} \tag{7}$$

where $\mathbf{F}_i^\alpha$ is the atomic force on the atom $i$ predicted by the NN potential $\alpha$, and $\overline{\mathbf{F}_i}$ is the average force on the atom $i$ over the four NN potentials.

Similarly to what was done in Ref. [25, 24] we have set up an empirical strategy to minimize the number of new DFT calculations. For this reason, we set a lower bound ($\sigma_l$) to the error $\sigma$ and an upper limit ($\sigma_u$) which is usually associated with nonphysical configurations in which atoms are too close or correspond to improbable chemistry. In detail, $\sigma_l$ was set to a value slightly higher than the average model deviation of the latest training set, while the choice of the $\sigma_u$ was based on the rule ([0.20 $\sim$ 0.30 ev/Å] + $\sigma_l$). The configurations with $\sigma > \sigma_u$ were outright rejected; the rest is divided into four intervals defined as follows (Fig. S4):
*a*) $0 < \sigma \leq \sigma_l - 0.05$
*b*) $\sigma_l - 0.05 < \sigma \leq \sigma_l$
*c*) $\sigma_l < \sigma \leq \sigma_l + 0.10$
*d*) $\sigma_l + 0.10 < \sigma \leq \sigma_u$
The intervals *c* and *d* are larger because the distribution of errors has a long tail. The configurations in *a* were automatically included among those that are described well by the NN model at this stage of the training. In the bins *b*, *c*, and *d* there will be $N_b$, $N_c$, and $N_d$ configurations and for these intervals we selected a fraction of configurations with percentages in the ratio $\sim 1 : 5 : 20$. The absolute values of these numbers were chosen to control the number of DFT calculations needed. Our rule favors selecting configurations in the *c* and *d* intervals that are most instrumental in expanding the variety of configurations added to the training data set. After this first iteration, a new NN was trained using the expanded data set. The error $\sigma$ associated with this NN was computed, and used as $\sigma$ for the new iteration.

**Step 3:** The DFT energies and forces of the configurations selected in step 2 were added to the training data set and the NN retrained.

Following our previous work [25], we updated the training set until the percentage of configurations in intervals *c* and *d* reached $\sim$ 10 % and remained almost unchanged for few other iterations. In the end, a total of $\sim 10^5$ atomic configurations were used.

### Validation of the NN model

The mean absolute errors (MAEs) of energies in the training and test set are 0.85 meV/atom and 0.90 meV/atom, respectively. The MAEs of forces in the training and test set are 37.59 meV/Å and 38.04 meV/Å, respectively. The test set consisted of $\sim$ 5700 configurations collected from the transition state regions of the reactions sampled in the NN-based OPES simulation at 750 K. We included in the test set configurations corresponding to the intermediates and transitions states of all the steps discussed in the main text. The comparison of DFT and the corresponding NN predicted atomic energies and forces over the test sets is given in Fig. S5. Furthermore, we analysed the MAEs for two fundamental reaction steps: ammonia reaction on the (111) surface, and N-N bond formation (insets in Fig. S5).

## Acknowledgments

It is a pleasure to acknowledge the help of Valerio Rizzi in the initial stages of the simulation and useful discussions with Enrico Trizio and Marco Bernasconi. We are

grateful to Narjes Ansari for the help with the graphic. We thank Vanda Glezakou and Robert Schlögl for reading a preliminary version of the manuscript. MP would like to thank Robert Schlögl for sharing his insight into catalysis. This work closely reflects his vision. However, any error or misinterpretation is our own responsibility. This work was supported by funds from the AmmoRef project in the framework of the agreement between the Max Planck Institute and the Italian Institute of Technology. Computational resources were also provided by the Swiss National Supercomputing Centre (CSCS) under project ID *S*1134 and *S*1183.

## Authors' contributions

M.Y, U.R., and M.P. made substantial contributions to the design and implementation of the work and wrote the manuscript.

## Declarations

The authors declare no competing interests.

## Data availability

All the inputs and instructions to reproduce the results presented in this manuscript can be found in the PLUMED-NEST repository.

## Code availability

Results described in this manuscript have been obtained with publicly available software packages such as CP2K (https://www.cp2k.org), Quantum Espresso (https://www.quantum-espresso.org), Lammps (https://docs.lammps.org), Plumed (https://www.plumed.org) and DeePMD-kit (https://docs.deepmodeling.com/projects/deepmd).

## References

[1] Robert Schlögl. Heterogeneous catalysis. *Angewandte Chemie International Edition*, 54(11):3465–3520, 2015.

[2] Joshua W Makepeace, Thomas J Wood, Hazel MA Hunter, Martin O Jones, and William IF David. Ammonia decomposition catalysis using non-stoichiometric lithium imide. *Chemical Science*, 6(7):3805–3815, 2015.

[3] Thomas J Wood, Joshua W Makepeace, and William IF David. Isotopic studies of the ammonia decomposition reaction using lithium imide catalyst. *Physical Chemistry Chemical Physics*, 19(6):4719–4724, 2017.

[4] Ping Chen, Zhitao Xiong, Jizhong Luo, Jianyi Lin, and Kuang Lee Tan. Interaction of hydrogen with metal nitrides and imides. *Nature*, 420(6913):302–304, 2002.

[5] William IF David, Martin O Jones, Duncan H Gregory, Catherine M Jewell, Simon R Johnson, Allan Walton, and Peter P Edwards. A mechanism for non-stoichiometry in the lithium amide/lithium imide hydrogen storage reaction. *Journal of the American Chemical Society*, 129(6):1594–1601, 2007.

[6] Jianping Guo, Peikun Wang, Guotao Wu, Anan Wu, Daqiang Hu, Zhitao Xiong, Junhu Wang, Pei Yu, Fei Chang, Zheng Chen, et al. Lithium imide synergy with 3d transition-metal nitrides leading to unprecedented catalytic activities for ammonia decomposition. *Angewandte Chemie International Edition*, 127(10):2993–2997, 2015.

[7] Shreya Mukherjee, Surya V Devaguptapu, Anna Sviripa, Carl RF Lund, and Gang Wu. Low-temperature ammonia decomposition catalysts for hydrogen generation. *Applied Catalysis B: Environmental*, 226:162–181, 2018.

[8] Ilaria Lucentini, Xènia Garcia, Xavier Vendrell, and Jordi Llorca. Review of the decomposition of ammonia to generate hydrogen. *Industrial & Engineering Chemistry Research*, 60(51):18560–18611, 2021.

[9] Thomas J Wood and Joshua W Makepeace. Assessing potential supports for lithium amide-imide ammonia decomposition catalysts. *ACS Applied Energy Materials*, 1(6):2657–2663, 2018.

[10] Robert Juza and Karl Opp. Metallamide und metallnitride, 25. mitteilung. zur kenntnis des lithiumimides. *Zeitschrift für anorganische und allgemeine Chemie*, 266(6):325–330, 1951.

[11] T Noritake, H Nozaki, M Aoki, S Towata, G Kitahara, Y Nakamori, and S-I Orimo. Crystal structure and charge density analysis of li2nh by synchrotron X-ray diffraction. *Journal of Alloys and Compounds*, 393(1-2):264–268, 2005.

[12] Michael P Balogh, Camille Y Jones, JF Herbst, Louis G Hector Jr, and Matthew Kundrat. Crystal structures and phase transformation of deuterated lithium imide, $Li_2ND$. *Journal of Alloys and Compounds*, 420(1-2):326–336, 2006.

[13] Giacomo Miceli, Michele Ceriotti, Marco Bernasconi, and Michele Parrinello. Static disorder and structural correlations in the low-temperature phase of lithium imide. *Physical Review B*, 83(5):054119, 2011.

[14] Stephen Hull. Superionics: crystal structures and conduction processes. *Reports on Progress in Physics*, 67(7):1233, 2004.

[15] C Moysés Araújo, Andreas Blomqvist, Ralph H Scheicher, Ping Chen, and Rajeev Ahuja. Superionicity in the hydrogen storage material $Li_2NH$: Molecular dynamics simulations. *Physical Review B*, 79(17):172101, 2009.

[16] Giacomo Miceli, Michele Ceriotti, Stefano Angioletti-Uberti, Marco Bernasconi, and Michele Parrinello. First-principles study of the high-temperature phase of li2nh. *The Journal of Physical Chemistry C*, 115(14):7076–7080, 2011.

[17] Richard Car and Mark Parrinello. Unified approach for molecular dynamics and density-functional theory. *Physical review letters*, 55(22):2471, 1985.

[18] Jörg Behler and Michele Parrinello. Generalized neural-network representation of high-dimensional potential-energy surfaces. *Physical Review Letters*, 98(14):146401, 2007.

[19] Linfeng Zhang, Jiequn Han, Han Wang, Roberto Car, and EJPRL Weinan. Deep potential molecular dynamics: a scalable model with the accuracy of quantum mechanics. *Physical Review Letters*, 120(14):143001, 2018.

[20] Robert G Parr. *Density functional theory of atoms and molecules*. Springer, 1980.

[21] John P Perdew, Kieron Burke, and Matthias Ernzerhof. Generalized gradient approximation made simple. *Physical Review Letters*, 77(18):3865, 1996.

[22] Luigi Bonati and Michele Parrinello. Silicon liquid structure and crystal nucleation from *ab initio* deep metadynamics. *Physical Review Letters*, 121(26):265701, 2018.

[23] Haiyang Niu, Luigi Bonati, Pablo M Piaggi, and Michele Parrinello. *Ab initio* phase diagram and nucleation of gallium. *Nature Communications*, 11(1):1–9, 2020.

[24] Manyi Yang, Luigi Bonati, Daniela Polino, and Michele Parrinello. Using metadynamics to build neural network potentials for reactive events: the case of urea decomposition in water. *Catalysis Today*, 387:143–149, 2022.

[25] Manyi Yang, Tarak Karmakar, and Michele Parrinello. Liquid-liquid critical point in phosphorus. *Physical Review Letters*, 127(8):080603, 2021.

[26] Michele Invernizzi and Michele Parrinello. Rethinking metadynamics: from bias potentials to probability distributions. *The Journal of Physical Chemistry Letters*, 11(7):2731–2736, 2020.

[27] Michele Invernizzi, Pablo M Piaggi, and Michele Parrinello. Unified approach to enhanced sampling. *Physical Review X*, 10(4):041034, 2020.

[28] Joshua W Makepeace, Jake M Brittain, Alisha Sukhwani Manghnani, Claire A Murray, Thomas J Wood, and William IF David. Compositional flexibility in Li-N-H materials: implications for ammonia catalysis and hydrogen storage. *Physical Chemistry Chemical Physics*, 23(28):15091–15100, 2021.

[29] Joshua W Makepeace, Martin O Jones, Samantha K Callear, Peter P Edwards, and William IF David. In situ X-ray powder diffraction studies of hydrogen storage and release in the Li–N–H system. *Physical Chemistry Chemical Physics*, 16(9):4061–4070, 2014.

[30] Kiya Ogasawara, Takuya Nakao, Kazuhisa Kishida, Tian-Nan Ye, Yangfan Lu, Hitoshi Abe, Yasuhiro Niwa, Masato Sasase, Masaaki Kitano, and Hideo Hosono. Ammonia decomposition over CaNH-Supported Ni catalysts via an $NH_2$-vacancy-mediated Mars-van krevelen mechanism. *ACS Catalysis*, 11(17):11005–11015, 2021.

[31] Graeme Henkelman, Andri Arnaldsson, and Hannes Jónsson. A fast and robust algorithm for bader decomposition of charge density. *Computational Materials Science*, 36(3):354–360, 2006.

[32] Ping Chen, Zhitao Xiong, Jizhong Luo, Jianyi Lin, and Kuang Lee Tan. Interaction between lithium amide and lithium hydride. *The Journal of Physical Chemistry B*, 107(39):10967–10970, 2003.

[33] Brian M Hoffman, Dmitriy Lukoyanov, Dennis R Dean, and Lance C Seefeldt. Nitrogenase: a draft mechanism. *Accounts of Chemical Research*, 46(2):587–595, 2013.

[34] Lance C Seefeldt, Brian M Hoffman, John W Peters, Simone Raugei, David N Beratan, Edwin Antony, and Dennis R Dean. Energy transduction in nitrogenase. *Accounts of Chemical Research*, 51(9):2179–2186, 2018.

[35] Zisheng Zhang, Borna Zandkarimi, and Anastassia N Alexandrova. Ensembles of metastable states govern heterogeneous catalysis on dynamic interfaces. *Accounts of chemical research*, 53(2):447–458, 2020.

[36] Xiangcheng Shi, Xiaoyun Lin, Ran Luo, Shican Wu, Lulu Li, Zhi-Jian Zhao, and Jinlong Gong. Dynamics of heterogeneous catalytic processes at operando conditions. *JACS Au*, 1(12):2100–2120, 2021.

[37] Gerhard Ertl. Reactions at surfaces: from atoms to complexity (Nobel lecture). *Angewandte Chemie International Edition*, 47(19):3524–3535, 2008.

[38] Marie-Laure Bonnet, Marcella Iannuzzi, Daniel Sebastiani, and Jurg Hutter. Local disorder in lithium imide from density functional simulation and NMR spectroscopy. *The Journal of Physical Chemistry C*, 116(35):18577–18583, 2012.

[39] Giacomo Miceli, Clotilde S Cucinotta, Marco Bernasconi, and Michele Parrinello. First principles study of the $LiNH_2/Li_2NH$ transformation. *The Journal of Physical Chemistry C*, 114(35):15174–15183, 2010.

[40] PW Tasker, EA Colbourn, and WC Mackrodt. Segregation of isovalent impurity cations at the surfaces of MgO and CaO. *Journal of the American Ceramic Society*, 68(2):74–80, 1985.

[41] Joost VandeVondele, Matthias Krack, Fawzi Mohamed, Michele Parrinello, Thomas Chassaing, and Jürg Hutter. Quickstep: Fast and accurate density functional calculations using a mixed gaussian and plane waves approach. *Computer Physics Communications*, 167(2):103–128, 2005.

[42] Stefan Maintz, Volker L Deringer, Andrei L Tchougréeff, and Richard Dronskowski. Lobster: A tool to extract chemical bonding from plane-wave based DFT, 2016.

[43] Gareth A Tribello, Massimiliano Bonomi, Davide Branduardi, Carlo Camilloni, and Giovanni Bussi. PLUMED 2: New feathers for an old bird. *Computer physics communications*, 185(2):604–613, 2014.

[44] Paolo Giannozzi, Stefano Baroni, Nicola Bonini, Matteo Calandra, Roberto Car, Carlo Cavazzoni, Davide Ceresoli, Guido L Chiarotti, Matteo Cococcioni, Ismaila Dabo, et al. QUANTUM ESPRESSO: a modular and open-source software project for quantum simulations of materials. *Journal of physics: Condensed matter*, 21(39):395502, 2009.

[45] Paolo Giannozzi, Oliviero Andreussi, Thomas Brumme, Oana Bunau, M Buongiorno Nardelli, Matteo Calandra, Roberto Car, Carlo Cavazzoni, Davide Ceresoli, Matteo Cococcioni, et al. Advanced capabilities for materials modelling with Quantum ESPRESSO. *Journal of physics: Condensed matter*, 29(46):465901, 2017.

[46] Paolo Giannozzi, Oscar Baseggio, Pietro Bonfà, Davide Brunato, Roberto Car, Ivan Carnimeo, Carlo Cavazzoni, Stefano De Gironcoli, Pietro Delugas, Fabrizio Ferrari Ruffino, et al. Quantum espresso toward the exascale. *The Journal of chemical physics*, 152(15):154105, 2020.

[47] Giovanni Bussi, Davide Donadio, and Michele Parrinello. Canonical sampling through velocity rescaling. *The Journal of chemical physics*, 126(1):014101, 2007.

[48] Stefan Goedecker, Michael Teter, and Jürg Hutter. Separable dual-space gaussian pseudopotentials. *Physical Review B*, 54(3):1703, 1996.

[49] Christian Hartwigsen, Sephen Gœdecker, and Jürg Hutter. Relativistic separable dual-space gaussian pseudopotentials from h to rn. *Physical Review B*, 58(7):3641, 1998.

[50] Han Wang, Linfeng Zhang, Jiequn Han, and E Weinan. DeePMD-kit: A deep learning package for many-body potential energy representation and molecular dynamics. *Computer Physics Communications*, 228:178–184, 2018.

[51] Steve Plimpton. Fast parallel algorithms for short-range molecular dynamics. *Journal of computational physics*, 117(1):1–19, 1995.

[52] Linfeng Zhang, Jiequn Han, Han Wang, Wissam Saidi, Roberto Car, et al. End-to-end symmetry preserving inter-atomic potential energy model for finite and extended systems. *Advances in Neural Information Processing Systems*, 31, 2018.

[53] Kaiming He, Xiangyu Zhang, Shaoqing Ren, and Jian Sun. Deep residual learning for image recognition. June 2016.

[54] Yuzhi Zhang, Haidi Wang, Weijie Chen, Jinzhe Zeng, Linfeng Zhang, Han Wang, and E Weinan. DP-GEN: A concurrent learning platform for the generation of reliable deep learning based potential energy models. *Computer Physics Communications*, 253:107206, 2020.